*Published in: Journal of Power Sources (2020), vol. 480, December, 229057*
*DOI: 10.1016/j.jpowsour.2020.229057*
*Status : Postprint (Author's version)*

# SPRAY-DRIED $K_3V(PO_4)_2/C$ COMPOSITES AS NOVEL CATHODE MATERIALS FOR K-ION BATTERIES WITH SUPERIOR ELECTROCHEMICAL PERFORMANCE

Jérome Bodart, Nicolas Eshraghi, Thomas Carabin, Bénédicte Vertruyen, Rudi Cloots, Frédéric Boschini, Abdelfattah Mahmoud*

*GREENMAT, CESAM Research Unit, Department of Chemistry, University of Liege, 4000, Liege, Belgium*

*Corresponding author. *E-mail address:* Abdelfattah.Mahmoud@uliege.be (A. Mahmoud).

**Keywords:** K-ion batteries ; Spray-drying synthesis ; Composites ; Cathode materials

**Graphical Abstract**

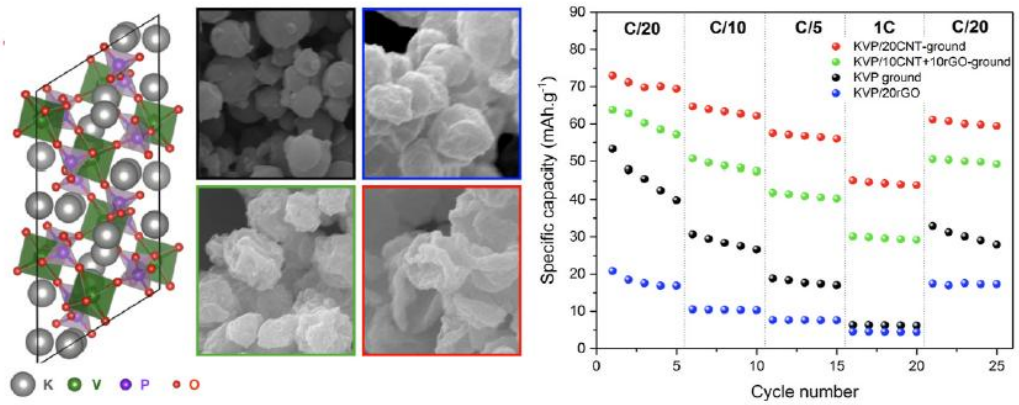


**Abstract**

Intensive efforts are needed to find an alternative to replace Li-ion batteries. Among the potential candidates, K- ions batteries (KIBs) have received a lot of interest thanks to the low reduction potential and low cost of potassium due to the high abundance and broad distribution of potassium sources. In this regard, the development of high performance cathode materials has raised some challenges. Phosphate-based materials are considered as the most promising cathode materials for KIBs owing to their high structural stability upon cycling, high ionic conductivity and high insertion potential. Here, $K_3V(PO_4)_2$ (KVP) and $K_3V(PO_4)_2/C$ composites are reported as new cathode materials for KIBs with a high theoretical capacity (150 $mAh.g^{-1}$) and a high working potential (3.5–4 V). The pristine KVP and KVP/C composite materials are obtained by spray-drying process. The influence of grinding process on the structural, morphological and the electrochemical properties is investigated. The composite with carbon nanotubes (KVP/20CNT) demonstrates the best reversible capacity of 101 $mAh.g^{-1}$ at C/ 40 using 0.8 M $KPF_6$ in PC +10 wt% FEC as electrolyte. Different characterization techniques are combined to investigate the structural and morphological properties of the materials such as XRD, SEM, TEM and Laser granulometry.

*Published in: Journal of Power Sources (2020), vol. 480, December, 229057*
*DOI: 10.1016/j.jpowsour.2020.229057*
*Status : Postprint (Author's version)*

# 1. Introduction

Our planet faces major sustainability challenges, demanding innovative research in various disciplines which include, among others, the field of energy storage technologies. Indeed, large-scale energy storage systems with long cycle life, high efficiency, low cost and excellent safety characteristics are urgently required to ensure the rapid shift from fossil-fuel-powered to clean energy sources.

Li-ion batteries (LIBs), which display the highest energy density compared to other technologies, have conquered the electronics field and are regarded as the best technology for powering mobile devices and electric vehicles. However, Li-ion batteries face many difficulties and limitations: in addition to safety concerns, the relative abundance of lithium is limited to 20 ppm in the Earth's crust and lithium resources are unevenly distributed leading to high extraction cost [1],[2]. These issues are raising doubts regarding the security of supply and cost of lithium in the future. For these reasons, intensive efforts are ongoing to find alternatives to replace Li-ion battery technology. Sodium, as one of the most abundant elements in the earth crust with only slightly higher reduction potential compared to lithium (+0.3 V vs Li), is an obvious candidate and research on Na-ion batteries (NIBs) has been a very active field for years [2]. Along with NIBs, potassium-ion batteries (KIBs) have recently been receiving a lot of interest: geographically well distributed, 880 times more abundant and 90% cheaper than lithium [2][3][4], potassium offers a reduction potential similar to lithium so that, for an equivalent specific capacity, KIBs should deliver higher energy density than NIBs. Besides, graphite (the commercial anode for LIBs since 1990) presents good performance for KIBs [2][5][6]. Thus, KIBs theoretically combine the advantages of LIBs and NIBs and are currently considered as strong candidates to replace LIBs for many applications including transportation and stationary applications [1][2][4].

In order to fulfill the promise of KIBs with high energy densities, the key issue is now the development of long life, high voltage and high capacity cathode materials. Breakthroughs in materials design/ processing are essential, by addressing the synthesis of new nanostructured composite positive electrode materials. Only a few cathode materials have been reported to date for KIBs and mainly four classes of electrode material families have attracted the attention of researchers in the recent years: i) organic compounds [7], ii) layered oxides [8], iii) Prussian blue analogues (PBAs) [9] or Prussian white analogues (PWAs) [10], and iv) polyanionic materials [5]. Among these materials, polyanionic materials are of high interest due to their high structural stability upon cycling, high insertion potential and good ionic conductivity. Only a few polyanionic materials such as $KFeSO_4F$, $K_3V_2(PO_4)_3/C$ and $K_3V_2(PO_4)_2F_3/C$ [5] have been investigated so far and the reported results suggest that the diffusion coefficient of $K^+$ ions is higher than those of $Li^+$ and $Na^+$ ions [11]. The crystallographic structure of polyanionic materials is characterized by a highly covalent three-dimensional framework generating large interstitial spaces and providing three-dimensional tunnels for fast ion diffusion. This is combined with a high theoretical specific capacity due to the multiple oxidation states of vanadium and iron ions, leading to good structural stability upon cycling [12][14]. However, their poor electronic conductivity needs to be addressed to remedy the low discharge/charge capacity and poor cycling performance especially at high cycling rates [15].

*Published in: Journal of Power Sources (2020), vol. 480, December, 229057*
*DOI: 10.1016/j.jpowsour.2020.229057*
*Status : Postprint (Author's version)*

Table 1 presents a non-exhaustive list of polyanionic compounds, mostly phosphates and pyrophosphates, recently investigated as cathode materials for K-ion batteries. The redox metal couples $Ti^{3+}/Ti^{4+}$, $Fe^{2+}/Fe^{3+}$ and $V^{3+}/V^{4+}/V^{5+}$ are characterized by working potentials of 1.5–2.5 V, 2.5–3.5 V and 3.5–4.5 V, respectively. These working potentials can be enhanced with the incorporation of fluorides in the structure [23]. The highest energy density is thus expected for vanadium-based compounds. However, most of the compounds in Table 1 are characterized by a relatively low theoretical capacity. One way to increase the theoretical capacity is to investigate candidates with lower molar mass or with a transition metal with multiple oxidation states (like vanadium). In this work, we propose $K_3V(PO_4)_2$ (KVP) as cathode material. Compared to $K_3V_2(PO_4)_3$ which has a theoretical capacity of 106 $mAh.g^{-1}$ for the extraction of one potassium for one vanadium, KVP has a higher K/V ratio leading to a higher theoretical specific capacity of 150 $mAh.g^{-1}$ for the extraction of two potassium for one vanadium. As such, KVP combines a high working potential of 3.5–4 V and a high theoretical capacity. KVP was first synthesized by Benhamada et al. in 1991 and the crystallographic structure was reported as monoclinic type in $P2_1/c$ space group [33], but it has never been investigated as a possible cathode material for K-ion batteries. The monoclinic structure is shown in Fig. 1. The potassium ions are positioned within the network formed by slightly distorted $VO_6$ octahedra sharing corners with phosphate tetrahedra.

**Table 1**
A non-exhaustive list of recently investigated polyanionic compounds as cathode materials for K-ion batteries.

| Materials | Structure | Theoretical capacity (mAh. $g^{-1}$) | Reported capacity (mAh. $g^{-1}$) | Discharge potential V *vs.* $K^+/K$ | Reference |
|---|---|---|---|---|---|
| Amorphous $FePO_4$ | – | 178 | 156 | 2.64 | [16] |
| $Fe_2(MoO_4)_3$ | Monoclinic anti-NASICON type ($P2_1$) | 91 ($1e^-$/Fe) | 78 | 2.6 | [17] |
| $K_2$ [$(VO)_2(HPO_4)_2(C_2O_4)$] | Triclinic $P\bar{1}$ | 109 ($1e^-$/V) | 81 | 3.5–4.1 | [18] |
| $K_{3-x}Rb_xV_2(PO_4)_3$/C | NASICON-type structure tetragonal ($P4_2/mnm$) | 97 | 55.70 | 3.75 | [19] |
| $K_3V_2(PO_4)_2F_3$ | NASICON-type structure tetragonal ($P4_2/mnm$) | 115 ($1e^-$/V) | 100 | 3.7 | [20] |
| $K_3V_2(PO_4)_3$/C | NASICON-type structure tetragonal ($P4_2/mnm$) | 106 ($1e^-$/V) | 90 | 3.7 | [21] |
| | | | 54 | 3.6–3.9 | [22] |
| $KFePO_4$/C | Triphylite-type structure Orthorhombic ($Pnma$) | 141 | 25 | 3 | [23] |
| $KFeSO_4F$ | Layered Monoclinic ($C2/c$) | 128 | 50 (*vs.* Li) | 3.5 (*vs.* Li) | [24] |
| | | | 100 | 4 | [25] |
| $KMnPO_4$/C | Triphylite-type structure Orthorhombic ($Pnma$) | 141 | 30 | 3 | [23] |
| $KMoP_2O_7$ | $KAlP_2O_7$-type monoclinic ($P2_1/c$) | 87 | 25 | 2.9 | [26] |
| $KTi_2(PO_4)_3$/C | NASICON-type structure tetragonal ($P4_2/mnm$) | 128 | 80 | 1.6 | [22] |
| $KTiP_2O_7$ | $KAlP_2O_7$-type monoclinic ($P2_1/c$) | 102 | 9.2 | 2.5 | [26] |
| $KVOPO_4$ | $KTiOPO_4$-type structure ($Pna2_1$) | 133 | 54 | 4 | [27] |
| | | | 115 | 4 | [18] |
| | | | 84 | 4 | [28] |
| $KVP_2O_7$ | $KAlP_2O_7$-type monoclinic ($P2_1/c$) | 102 | 61 | 4.2 | [26] |
| $KVPO_4F$ | $KTiOPO_4$-type structure ($Pna2_1$) | 131 | 92 | 4 | [28] |
| | | | 111 (*vs.* Li) | 4.2 (*vs.* Li) | [29] |
| | | | 125 (*vs.* Li) | 4.05 (*vs.* Li) | [30] |
| | | | 105 | 4.3 | [31] |
| | | | 80 | 3.5–4 | [32] |
| **$K_3V(PO_4)_2$/C** | **Monoclinic ($P2_1/c$)** | **150 ($2e^-$/V)** | **101** | **3.5** | **This Work** |

In the present work, $K_3V(PO_4)_2$ and $K_3V(PO_4)_2$/C cathode materials were prepared using spray-drying route. This synthesis method is easy, inexpensive and suitable for obtaining complex multi-component powders with a high degree of homogeneity required for very good electrochemical properties [34]. To synthesize

*Published in: Journal of Power Sources (2020), vol. 480, December, 229057*
*DOI: 10.1016/j.jpowsour.2020.229057*
*Status : Postprint (Author's version)*

the pure $K_3V(PO_4)_2$ material, different temperatures and durations for the heat treatment were tested. To ensure adequate electronic conductivity especially when the electrode was cycled at high rate, the precursors were mixed with different carbon allotropes (graphene oxide: GO and carbon nanotubes: CNT) during the material synthesis, leading to carbon/active material composite blends at the nanometric level for $K_3V(PO_4)_2$/C composite cathodes. The good mixture of the electrode material and carbon would increase the electronic conductivity and induce a positive impact on the electrochemical properties as it has already been shown for Na-ion batteries[13][15]. The particle size and morphology of the electrode materials have also significant influence on the electrochemical properties [13][15]; thus, the prepared materials were then subjected to ball-milling to decrease the particle size and enhance $K^+$ ion diffusion in the electrode during charge/discharge process. The thermal behavior and decomposition of the spray-dried precursor were analyzed using TGA/DSC technique. The structural and morphological properties of the prepared materials were systematically investigated by combining XRD, SEM, TEM, BET and laser granulometry characterization techniques. The electrochemical performances were evaluated in half-cells by galvanostatic techniques and electrochemical impedance spectroscopy.

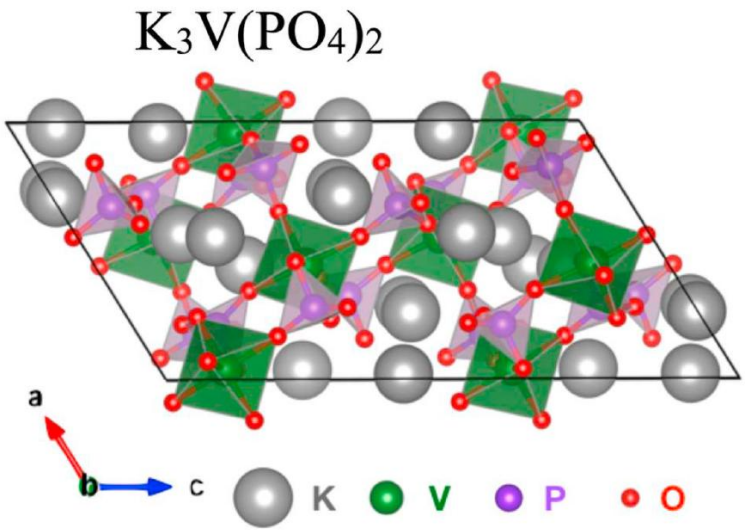


*Fig. 1. Representation of the monoclinic crystalline structure of potassium vanadium phosphate, $K_3V(PO_4)_2$ ($P2_1/c$ space group) with $VO_6$ octahedra (in green), $PO_4$ tetrahedra (in violet), oxygen atoms (as red spheres) and potassium atoms (as grey spheres).*

# 2. Experimental section

## 2.1. MATERIALS AND CHEMICALS

$V_2O_5$ powder (98% purity) was purchased from Sigma Aldrich. $NH_4H_2PO_4$ (99% purity) and KOH (99.95% purity) were purchased from Acros Organics. Ascorbic acid (99% purity) and citric acid (99.5% purity) were

*Published in: Journal of Power Sources (2020), vol. 480, December, 229057*
*DOI: 10.1016/j.jpowsour.2020.229057*
*Status : Postprint (Author's version)*

obtained from Alfa Aesar and used as received. The suspension of carbon nanotubes (Aquacyl AQ0302-nanocyl 3 wt%, NC7000 multiwall carbon nanotubes waterborne dispersion) was purchased from Nanocyl and the graphene oxide suspension (0.4 wt% in water) was obtained from Graphenea.

## 2.2. SYNTHESIS OF $K_3V(PO_4)_2$ (KVP) AND $K_3V(PO_4)_2$/C (KVP/C) MATERIALS

$K_3V(PO_4)_2$ and $K_3V(PO_4)_2$/C materials were prepared by the spray- drying method. Firstly, $V_2O_5$, $NH_4H_2PO_4$, citric acid ($C_6H_8O_7$) and ascorbic acid ($C_6H_8O_6$) in molar ratio 0.5/2/1/1 were dissolved and stirred in milliQ water (18.2MΩ.cm$^{-1}$) at 80 °C under argon atmosphere for 1 h to obtain a 0.1 M solution of precursors. Then, KOH was added to the solution in stoichiometric ratio followed by 1 h stirring at 80 °C. In the case of composite materials with carbon (KVP/C), suspensions were prepared with 20 wt% (vs. total mass of KVP precursors) of either CNT or GO (for KVP/20CNT and KVP/20rGO) or a mix of 10 wt% of CNT + 10 wt% of GO (for KVP/10CNT+10rGO) added to the KVP precursor solution. After cooling down to room temperature, the solution or suspensions were injected in a semi industrial spray-dryer (GEA-Niro Mobile Minor using a bi-fluid nozzle injection mode). Spray-drying was carried out under an air pressure of 3 bars with a 25 ml min$^{-1}$ feed rate, an inlet temperature of 240 °C and an outlet temperature of 120 ± 1 °C. The collected powders were immediately stored at 60 °C to minimize the contact with humidity. The effect of the heat treatment temperature and duration on crystalline phase formation was investigated to determine the optimized conditions to obtain pure materials. The spray-dried powders were submitted to heat treatment at different temperatures and durations under argon atmosphere with a heating rate of 150 °C.h$^{-1}$. The powders (2.5 g) were then placed with 0.5 mm diameter zirconia balls (50 g) and 25 ml isopropanol in zirconia grinding jars and were ground at 375 rpm during different durations from 30 to 120 min (by steps of 30 min) using a planetary mill (Retsch PM400/2, alternate rotation mode) followed by drying at 70 °C for 24 h.

## 2.3. THERMAL, STRUCTURAL AND MORPHOLOGICAL CHARACTERIZATIONS.

In order to optimize the synthesis process of the KVP material, the thermal behavior of the spray-dried KVP powder was analyzed by thermogravimetric analysis (TGA) using a Q100 system from TA instruments. About 10 mg of each sample was placed in an alumina crucible and heated under argon from room temperature to 800 °C at a heating rate of 20K.min$^{-1}$ to yield the onset decomposition temperature.

X-ray diffraction (XRD) was carried out to identify the obtained phases over the 2θ range from 9° to 50° with a Bruker D8 Twin-Twin powder diffractometer using Cu Kα radiation. The cell parameters were refined with TOPAS software [35], using the $P2_1/c$ space group and atomic positions proposed by Benhamada et al. [33] Crystallite size (CS) was evaluated using the Scherrer formula CS = 0.9 λ/(β cos θ), where λ is the wavelength, β is the full width at half maximum of the (123) peak and θ is the Bragg angle of diffraction.

The microstructures of the KVP and KVP/C materials were examined using a scanning electron microscope FEG-SEM (XL 30, FEI) operated at 15 kV and a transmission electron microscope TECNAI G2 TWIN (FEI) operating at 200 kV. Measurements of specific surface area and texture properties, including analysis of

*Published in: Journal of Power Sources (2020), vol. 480, December, 229057*
*DOI: 10.1016/j.jpowsour.2020.229057*
*Status : Postprint (Author's version)*

porosity for all the samples (KVP and KVP/C), were determined through measuring nitrogen ($N_2$) adsorption–desorption isotherms with a Micromeritics ASAP 2020 Plus system. Samples were degassed at 150 °C for 6 h prior to analysis.

The evolution of the particle size distribution of the powders during ball-milling was followed by laser granulometry using a Mastersizer 2000 Malvern system.

## 2.4. ELECTROCHEMICAL CHARACTERIZATIONS

Electrochemical measurements of KVP and KVP/C as cathode materials for K-ion batteries were conducted in two-electrode coin cells. The composite electrodes were prepared by mixing 70 wt% of KVP powder as active material with 20 wt% carbon black as electronic conductor and 10 wt % polyvinylidene fluoride (PVDF) as binder dissolved in n-methyl pyrrolidinone (NMP). In the case of KVP/C samples, the carbon content was first measured with a carbon analyzer (Multi EA 4000, Analytik Jena) at 1200 °C with an oxygen flow in order to determine the exact quantity of CNT and/or rGO in the composite material. The quantity of KVP and carbon was then adapted to reach the ratio 70/20/10 (KVP/C/PVDF). Each suspension was mixed in a 50 ml volume jar with 5 mm diameter zirconia balls at 250 rpm during 1 h. The resulting slurry was then coated on a 25 μm thick aluminum foil as current collector by the Doctor blade method followed by drying at 110 °C under vacuum for 12 h. Electrodes were cut into 15 mm diameter discs with active mass loading of approximately 1–2 mg. Coin cells were assembled in an argon-filled glove box using a glass microfiber paper (Whatman GF/A) as separator, 0.8 M $KPF_6$ +10 wt% of fluoroethylene carbonate (FEC) dissolved in propylene carbonate (PC) as electrolyte, and potassium foil as the counter and reference electrodes. All cells were tested within a fixed voltage window, between 2.0 and 4.5 V vs. $K^+/K$, under galvanostatic conditions at different current density rates: C/40 - 1 C (1C corresponds to the extraction/insertion current of 1 K/KVP in 1 h). All electrochemical tests were carried out at room temperature using a Neware BTS4000 Electrochemical Test System.

Electrochemical Impedance Spectroscopy (EIS) experiments were performed in 3 electrodes Swagelok-type cells, the electrodes were prepared as mentioned before for working electrode, metallic potassium was used both as counter and reference electrode. The electrolyte and separators were the same as for cycling experiments. The EIS analyses were performed at room temperature at open circuit voltage (OCV)

($E_{OCV}$ = ~2.9 V) in the frequency range from 1 MHz to 10 mHz with 5 mV amplitude using a VMP3 Bio-Logic potentiostat. EIS data were analyzed by a non-linear least-square (NLLSQ) fit software developed by B.A. Boukamp [36]. The equivalent circuit used to fit the data was $R_e + (R_{CT}.Q)/Q$ where $R_e$ is the electrolyte resistance, $R_{CT}$ is the charge transfer resistance and Q is a constant phase element (CPE) replacing the double layer capacity.

The cyclic voltammetry tests were performed in two-electrode coin cells (with the same electrode preparation method as explained before) at different scan rates from 0.1 to 0.5 mV $s^{-1}$. The tests were realized using a VMP3 Bio-Logic potentiostat.

*Published in: Journal of Power Sources (2020), vol. 480, December, 229057*
*DOI: 10.1016/j.jpowsour.2020.229057*
*Status : Postprint (Author's version)*

# 3. Results and discussion

## 3.1. SYNTHESIS AND CHARACTERIZATION OF KVP

Thermogravimetric analysis (TGA) and differential scanning calorimetry (DSC) are widely used characterization techniques to evaluate the thermal behavior and the effects of heat treatment on the material degradation and crystallization [37]. Here, we used TGA/DSC analyses to optimize the synthesis conditions (temperature of formation) of the KVP material, by following the variation of the sample mass when heating up the spray-dried powder from room temperature to 800 °C under argon.

The TGA and derivative thermogravimetric (DTG) curves are presented in Fig. 2a. The data show a continuous mass loss between 25 °C and 600 °C. The powder undergoes a mass loss (0.31 wt%) up to 100 °C (corresponding to a small peak observed in the DTG curve) which is due to the elimination of the water in the powder. Then, two significant weight losses are detected at 180 °C and 400 °C associated with the degradation of the precursors used for the preparation of the material. Indeed, the degradation of $NH_4H_2PO_4$ and potassium citrate/ascorbate have been reported to start at 160 °C and at 225 °C, respectively [38][39]. The complete degradation of the precursors occurs at 600 °C leading to a total mass loss of 31%. At 600 °C, the TG curve stabilizes with no further decrease denoting the formation of KVP. Consequently, 600 °C is the lowest temperature to synthesize the KVP phase.

The DSC profile obtained in the temperature range of 25–800 °C under the dynamic atmosphere of argon is shown in Fig. 2b.

The DSC curve displays mainly 3 peaks at 180, 650 and 758 °C corresponding to the endothermic/exothermic processes during the heat treatment. The endothermic peak observed at 180 °C corresponds to the degradation of $NH_4H_2PO_4$ precursor, in good agreement with TGA results. The two exothermic peaks detected at 650 °C and 758 °C are related to the crystallization and/or degradation of KVP.

*Published in: Journal of Power Sources (2020), vol. 480, December, 229057*
*DOI: 10.1016/j.jpowsour.2020.229057*
*Status : Postprint (Author's version)*

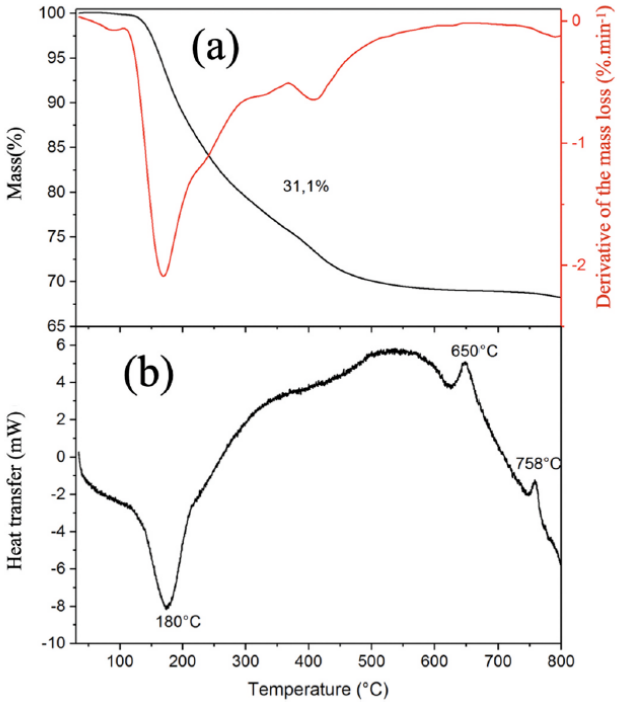


*Fig. 2. (a) TGA profile and its derivative curve, (b) DSC curve of the spray- dried precursor of the KVP powder.*

## 3.2. CRYSTAL STRUCTURE OF SYNTHESIZED KVP

The spray-dried KVP powder was subjected to different heat treatments at 550, 600, 650, 700 and 750 °C during 1, 8 and 16 h under argon, in order to investigate the KVP formation in relation with the key temperatures detected by TGA/DSC analyses. The X-ray diffraction patterns of the KVP samples are shown in Fig. 3a.

The XRD pattern of the sample prepared at 550 °C during 8 h displays an amorphous phase which confirms that 550 °C is not sufficient to obtain pure crystallized KVP. On the contrary, temperatures of 600 °C or 650 °C are high enough to obtain the pure and crystalline KVP material. All the XRD peaks of the powder prepared at 650 °C during 8 h can be indexed in the monoclinic structure with space group $P2_1/c$ (04-011-3486-PDF) proposed by Benhamada et al. [33]. The cell parameters were refined to values of a = 9.573 ± 0.002 Å, b = 11.146 ± 0.002 Å, c = 18.129 ± 0.004 Å and β = 121.75 ± 0.02°, in good agreement (i.e., difference below 0.5%) with the originally reported values. The atomic positions and occupation factors were not refined since the structure model includes 28 independent atoms, all on general positions, so that a reliable refinement was not possible for our datasets obtained with a laboratory powder diffractometer. However, the atomic positions and occupation factors taken from the published structure [33] provide a decent fit with the experimental data (see Fig. S1). This confirms that 650 °C is high enough to obtain the KVP-material with high purity and good crystallinity. The KVP material was pyrolyzed at 650 °C (highest temperature) in

*Published in: Journal of Power Sources (2020), vol. 480, December, 229057*
*DOI: 10.1016/j.jpowsour.2020.229057*
*Status : Postprint (Author's version)*

order to maximize the crystallinity of the material. Further increase of the pyrolysis temperature from 650 to 700 °C or 750 °C leads to the degradation of KVP and the formation of pyrophosphates as secondary phase. The evolution of the XRD patterns of KVP prepared at 650 °C with the pyrolysis time is illustrated in Fig. 3b.

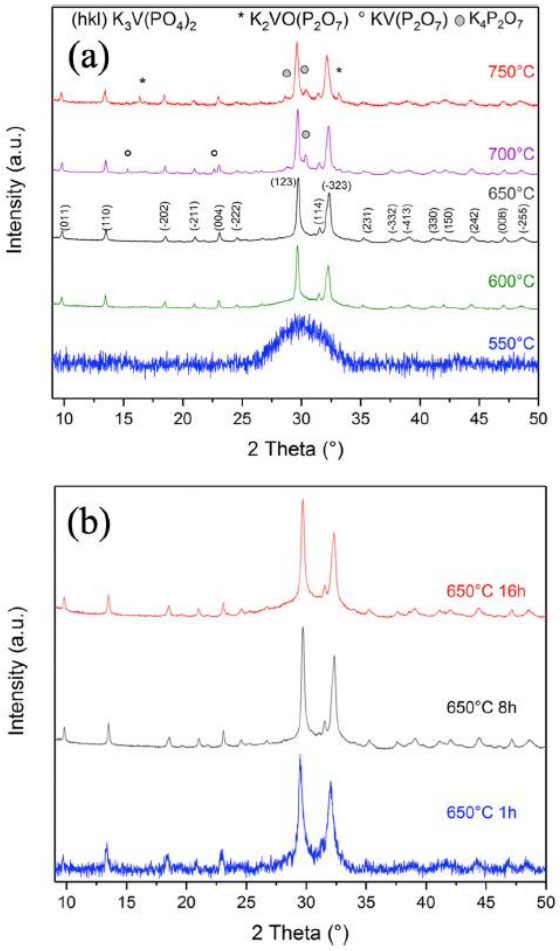


*Fig. 3. (a) XRD patterns of $K_3V(PO_4)_2$ samples prepared at different pyrolysis temperatures during 8 h under argon and (b) at different durations at 650 °C under argon.*

The XRD patterns display lower crystallinity after 1 h of pyrolysis as compared to 8 and 16 h. The increase of the pyrolysis duration from 8 to 16 h has no obvious effect on the KVP structure and shows the good thermal stability of the synthesized KVP samples. To summarize, the optimal conditions to obtain high purity and well crystalized KVP powder are 650 °C during 8 h. These conditions were applied to KVP and KVP/C powders studied in terms of microstructure and electrochemical properties.

## 3.3. MORPHOLOGICAL CHARACTERIZATION OF KVP

The SEM micrographs of the spray-dried KVP powders before and after pyrolysis at 650 °C during 8 h under argon atmosphere are presented in Figs. S2a and S2b. Before pyrolysis, the spray-dried particles are

*Published in: Journal of Power Sources (2020), vol. 480, December, 229057*
*DOI: 10.1016/j.jpowsour.2020.229057*
*Status : Postprint (Author's version)*

constituted of a homogeneous mixture of precursor nanoparticles forming dense spherical particles with a smooth surface and an average particle size of 2 μm.

After pyrolysis, the particles remain spherical with the same size but with a rough surface. The surface roughness is mainly due to the decomposition of precursors at the surface in favor of formation of the crystalized phase (in good agreement with XRD result). The BET technique was used to measure the specific surface area of the heat-treated material. The KVP powder exhibits a small specific surface area of 1.7 $m^2 g^{-1}$ due to the large size and low porosity of spherical particles.

## 3.4. ELECTROCHEMICAL PERFORMANCE OF KVP MICROPARTICLES

In this section, electrochemical performance of spray-dried KVP was assessed by galvanostatic charge-discharge cycling in half-cell configuration in the voltage range 2–4.5 V vs. $K^+/K^0$. Indeed, the spray-dried KVP is evaluated as a candidate material for cathode in KIBs, since phosphate-based materials demonstrate high mobility of the $K^+$ ions during the extraction/intercalation process in 3D open-framework structures [23]. Fig. S3a presents the charge/discharge voltage profiles of the first 3 cycles of KVP electrode at C/40. During charge, the voltage profile between 2 and 3.5 V has a steep slope with no clear plateau followed by a pseudo plateau between 3.5 and 4 V, and finally a continuous increase in voltage with $K^+$ ion extraction is observed. Reversible phenomena are observed during the discharge process. A comparable reaction mechanism was reported for $KVPO_4F$ material when used as cathode material for K-ion battery [31]. The cell delivers low initial charge and discharge capacities of 45 and 30 $mAh.g^{-1}$ corresponding to 30% and 20% of the theoretical capacity (150 $mAh.g^{-1}$), respectively. Then, the capacity decays after the first cycle which is accompanied by the decrease of the operating voltage due to polarization. Fig. S3b presents the evolution of the discharge and charge capacity vs. cycle number at C/40 rate for KVP cathode. The discharge capacities decrease during the first 4 cycles and reach around 25 $mAh.\ g^{-1}$, then stabilizes for the 20 subsequent cycles. This low electrochemical performance is associated with the low specific surface area of the microspheres and a low intrinsic electronic conductivity of the KVP phase. To improve the electrochemical performances of the material, it is therefore necessary to increase the electronic conductivity of the KVP particles and/or reduce the particle size [13][15].

## 3.5. EFFECT OF THE ADDITION OF CONDUCTIVE CARBON ON THE STRUCTURAL, MICROSTRUCTURAL AND ELECTROCHEMICAL PROPERTIES OF KVP/C COMPOSITE

In order to enhance the electrochemical performance of the KVP material, two solutions were considered. The first one is to grind the materials to decrease the size of the particles and thereby to reduce the electron diffusion path during the charge/discharge process. Another solution is to incorporate conductive carbon in the structure to prepare composite materials. This carbon addition should enhance the electrochemical performance by helping to solve the issue of the low electronic conductivity of the phosphate-based material. The addition of carbon to the precursor solution was chosen as the first approach to study in this work, since spray-drying process is highly compatible to fabrication of multicomponent mixtures. Three KVP/C composite materials were prepared by addition of 20 wt% of CNT (KVP/20CNT), 20 wt% of GO

*Published in: Journal of Power Sources (2020), vol. 480, December, 229057*
*DOI: 10.1016/j.jpowsour.2020.229057*
*Status : Postprint (Author's version)*

(KVP/20rGO) and 10 wt% of CNT + 10 wt% of GO (KVP/ 10CNT+10rGO) to the KVP precursor solution. The GO is reduced during the heat treatment leading to reduced graphene oxide (rGO). The XRD patterns of KVP, KVP/20CNT, KVP/20rGO and KVP/10CNT+10rGO are shown in Fig. 4a.

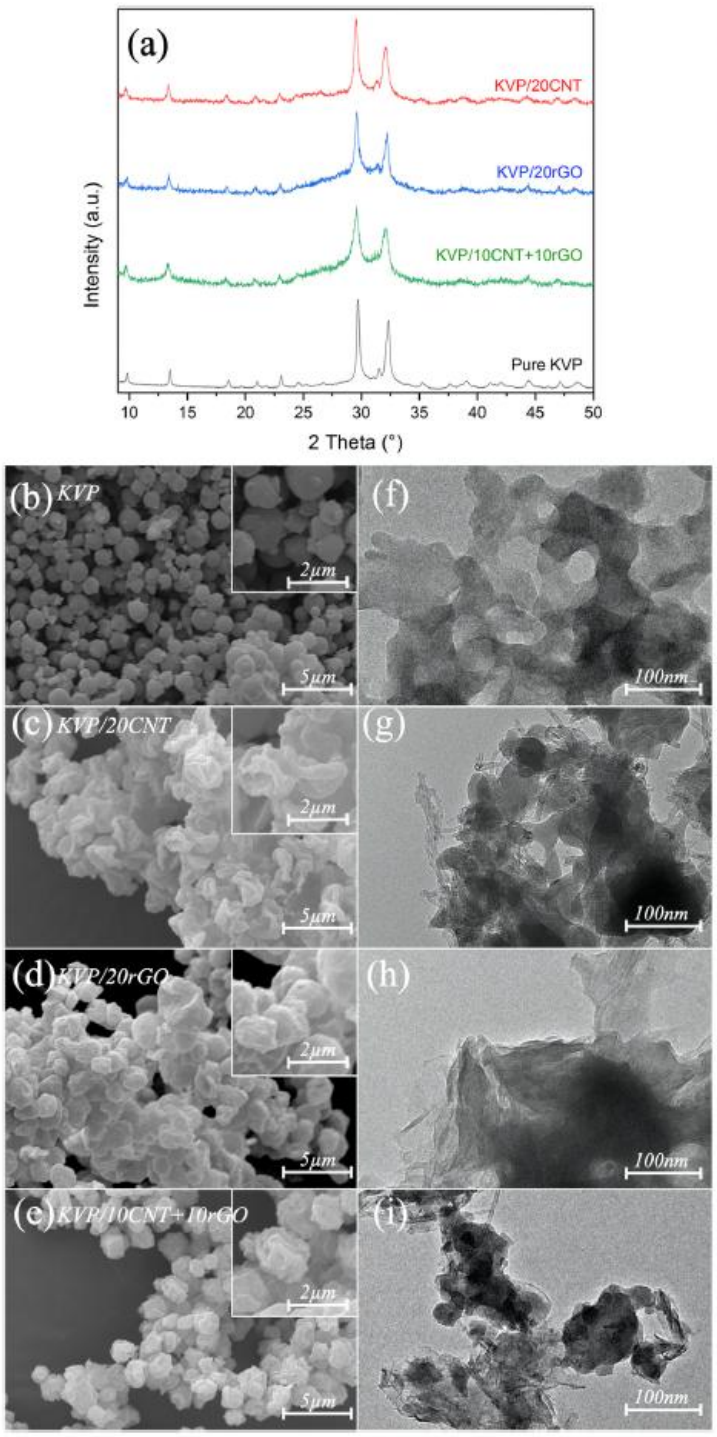


**Fig. 4.** (a) XRD patterns of pure KVP, KVP/20CNT, KVP/20rGO and KVP/10CNT+10rGO samples prepared by spray-drying method and pyrolyzed at 650 °C during 8 h under argon. SEM micrographs of (b) KVP, (c) KVP/20CNT, (d) KVP/20rGO and (e) KVP/10CNT+10rGO prepared by spray-drying with carbon allotropes added in solution and pyrolyzed at 650 °C during 8 h under argon (higher magnification in the inset). TEM micrographs of (f) KVP, (g) KVP/20CNT, (h) KVP/20rGO and (i) KVP/10CNT+10rGO prepared by spray-drying and pyrolyzed at 650 °C during 8 h under argon.

*Published in: Journal of Power Sources (2020), vol. 480, December, 229057*
*DOI: 10.1016/j.jpowsour.2020.229057*
*Status : Postprint (Author's version)*

All the peaks can be indexed in the monoclinic structure with space group $P2_1/c$ with no crystalline impurity in the synthesized KVP/C composite materials. Carbon addition does not affect the purity of the KVP phase, however, small differences in XRD pattern upon carbon addition are observed. A broad bump appears between 25° and 35° in the background of the XRD pattern and the diffraction peaks become broader. The bump between 25° and 35° can be attributed to the carbon [40][41][42].The broader peak shape of the KVP reflections is attributed to a smaller crystallite size. Table 2 presents the crystallite size of KVP and KVP/C materials as calculated using the Scherrer formula. The crystallites size decreases with carbon addition from 39 nm for KVP to 31 nm for KVP/20rGO, 26 nm for KVP/10CNT and 23 nm for KVP/10CNT+10rGO. This phenomenon has already been observed and suggests difference in crystallite growth mechanism for KVP material with the presence of the carbon nanotubes and graphene oxide [43]. This result could be attributed to two possible reasons: a higher number of nucleation sites and/or the geometric constraints due to the rigidity of carbon. [13][44][45].

**Table 2**
Crystallite size of KVP, KVP/20CNT, KVP/20rGO and KVP/10CNT+10rGO samples before and after grinding.

| Samples | Average crystallite size (nm) | |
|---|---|---|
| | Before grinding | After grinding |
| KVP | 39 ± 3 | 13 ± 4 |
| KVP/20CNT | 26 ± 1 | 16 ± 6 |
| KVP/20rGO | 31 ± 2 | 30 ± 2 |
| KVP/10CNT+10rGO | 23 ± 1 | 19 ± 8 |

The effect of carbon addition on the microstructure of KVP was studied by combining scanning electron microscopy (SEM) and transmission electron microscopy (TEM). Fig. 4b, c, 4d, 4e present the SEM micrographs of KVP, KVP/20CNT, KVP/20rGO and KVP/10CNT+10rGO powders respectively and Fig. 4f, g, 4h, 4i present the corresponding TEM images. The addition of CNT leads to the formation of collapsed particles with flattened morphology characterized by high particle size of 2.5 μm. The addition of carbon nanotubes and their high mechanical strength leads to the buckling of the particles. The first step during the drying process by spray-drying is the formation of a viscoelastic shell due to the aggregation induced by the solvent flow [46]. During the drying of the droplets multiple depressions are formed leading to wrinkled shape. With the reduction of volume these wrinkles overlap leading to highly deformed shapes [15]. The CNT are well dispersed at the surface and inside of the KVP particles, forming a strong CNT network as shown in Fig. 4g. In comparison with KVP (Fig. 4b), KVP/20rGO and KVP/10CNT+10rGO show particles with semi-spherical shape and slight deformation at the surface of the secondary particles (Fig. 4e and f). The quasi-spherical shape of the particles was not deteriorated due to the good dispersion of the graphene layer at the surface of the KVP materials. As observed in TEM images (Fig. 4h and i), KVP was successfully covered by reduced graphene oxide flakes for KVP/20rGO and rGO and CNT for KVP/10CNT+10rGO. It turns out that, for all KVP/C materials, carbon is uniformly distributed amongst and at the surface of the KVP particles for the CNT (Fig. 4g and i) and surrounding the surface of the particles for the rGO (Fig. 4h and i and Fig. S4).

The specific surface area increased hugely with addition of 20 wt% CNT to 36.8 $m^2 g^{-1}$ as compared to 1.8 $m^2 g^{-1}$ in pristine KVP (Table S1). This is attributed to a combination of the large specific surface area of the

*Published in: Journal of Power Sources (2020), vol. 480, December, 229057*
*DOI: 10.1016/j.jpowsour.2020.229057*
*Status : Postprint (Author's version)*

CNT themselves with the increase of specific surface area of KVP reflected in the smaller crystallite size detected by XRD. The electron microscopy results show that the CNTs are well deagglomerated and well dispersed at the surfaces of the KVP particles (Fig. 4c and g). This increase in specific surface area is favorable for $K^+$ ions diffusion by the increase of the active surface of the material that contributes in the electrochemical reaction. In the case of the GO addition, the specific surface of 6.6 $m^2 g^{-1}$ is only moderately higher than the carbon free KVP, probably because the rGO sheets wrap around the KVP particles. This should increase the conductivity at the surface of the particle and also improve the electrochemical performance due to the easier movement of electrons. In the case of the mixed composite, we obtain a value of 11.2 $m^2 g^{-1}$ intermediate between KVP/20CNT and KVP/20rGO. These results suggest that the most promising electrochemical performance should be displayed by KVP/10CNT+10rGO thanks to combining the positive effects of the two carbon allotropes in terms of surface area and electronic conductivity.

The effect of the carbon addition on the electrochemical properties of KVP and KVP/C cathode materials for K-ion batteries were studied by galvanostatic measurements at C/40 in the voltage range of 2–4.5 V. Fig. 5a–d presents the charge/discharge profiles of KVP and KVP/C in the first 3 cycles. The cycling performance for 10 cycles is presented in Fig. 5e, indicating clearly that the addition of conductive carbon improves the electrochemical performance of KVP/C cathodes and allowed to enhance the discharge capacities in comparison with the KVP material. Indeed, KVP/20CNT, KVP/20rGO and KVP/10CNT+10rGO present higher initial discharge capacities compared to 30 $mAh.g^{-1}$ for KVP with delivering 45, 60 and 101 $mAh.g^{-1}$, respectively. This result is due to the uniform distribution of KVP particles in the carbon matrix (CNT and rGO) and high surface area of KVP/C materials that reduce the electronic diffusion lengths during the charge/discharge process and increase the electrochemical performance. It is also important to indicate that the type of carbon allotrope plays a key role in enhancing the electrochemical properties in KVP/C.

This is in good agreement with previous results reported in the literature [13][15], highlighting the interest of the carbon addition to the phosphate-based electrode materials for rechargeable batteries. KVP/10CNT+10rGO demonstrates the highest capacity over 10 cycles which is associated with lower polarization between the charge and discharge curves during cycling. This is due to the combined positive effect of the CNT and rGO on electronic conductivity. This is also due to the open framework of the KVP structure that permits a rapid transport of $K^+$ ions and leads to a high ionic conductivity [23].

This observation confirms that improvement in electron transport is achieved by carbon addition during the spray-drying preparation of the KVP/C composite material. Electrochemical impedance spectroscopy (EIS) tests were performed to investigate the influence of carbon addition on electrochemical performance of KVP material [47][48]. The Nyquist plots of KVP and KVP/C electrodes recorded at OCV before galvanostatic cycling are presented in Fig. 5f. The equivalent circuit model used for the analysis of the impedance spectra is presented in the Fig. S5. EIS data were analyzed by the non-linear least-square (NLLSQ) fit software developed by B.A. Boukamp [36]. All electrodes show similar impedance spectra formed by a semicircle at high frequency and a line at low frequency corresponding to diffusion phenomenon. $R_e(R_{CT}.Q)Q$ equivalent circuit was used to analyze the different spectra and extract the resistance of the electrolyte $R_e$ (intercept of the curve on the $R_e(Z)$ axis in the high frequency region) and the resistance of charge transfer $R_{CT}$. The different values are summarized in Table 3.

*Published in: Journal of Power Sources (2020), vol. 480, December, 229057*
*DOI: 10.1016/j.jpowsour.2020.229057*
*Status : Postprint (Author's version)*

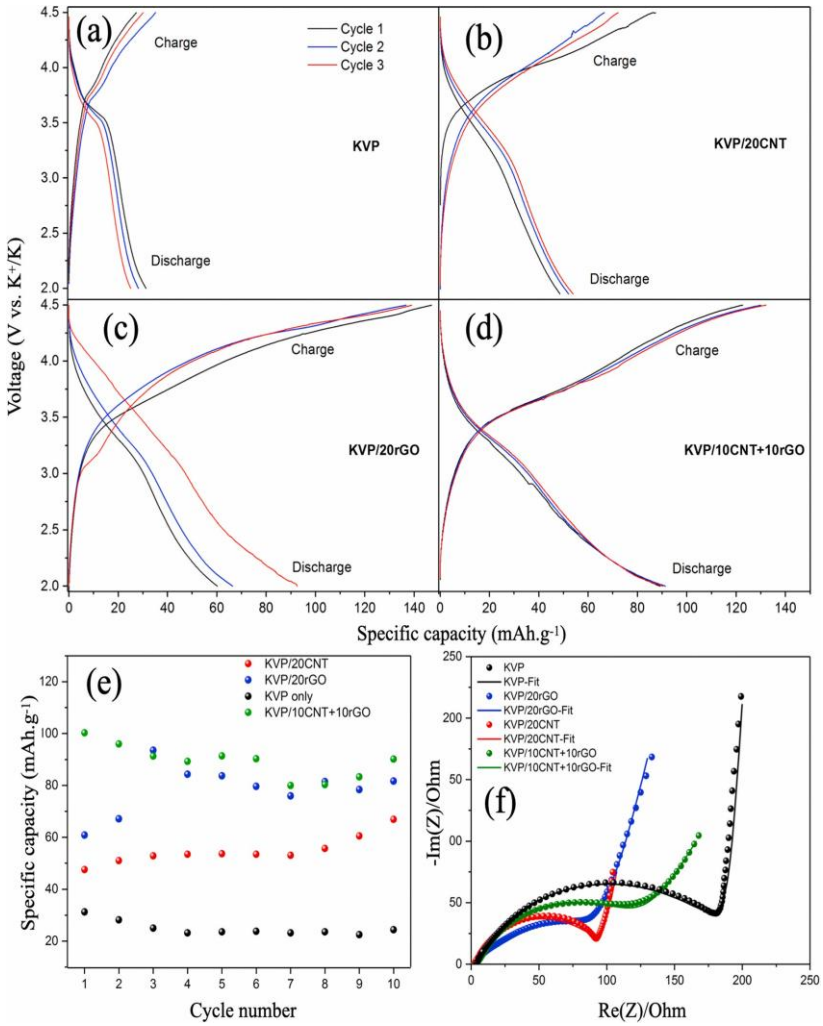


***Fig. 5.*** *Charge/discharge curves of the first 3 cycles of (a) KVP, (b) KVP/20CNT, (c) KVP/20rGO and (d) KVP/10CNT+10rGO and (e) Cycling performance of KVP and KVP/C electrodes at room temperature at C/40. The voltage window explored was 2.0–4.5 V, (f) Nyquist plots of KVP, KVP/20CNT, KVP/20GO and KVP/ 10CNT+10GO and their corresponding fitted curve.*

**Table 3**
Calculated resistances by fitting using equivalent circuit for both electrolyte resistance $R_e$ and charge transfer resistance $R_{CT}$ of KVP and KVP/C electrode materials.

| Samples | $R_e$ (Ω) | $R_{CT}$(Ω) |
|---|---|---|
| KVP | 3.7 ± 2 | 187.6 ± 5 |
| KVP/20CNT | 3.1 ± 2 | 92.9 ± 8 |
| KVP/20rGO | 2.5 ± 3 | 99.3 ± 10 |
| KVP/10CNT+10rGO | 5.5 ± 3 | 113.8 ± 26 |
| KVP/20rGO - Ground | 5.6 ± 3 | 189.2 ± 19 |

Published in : ORTHO-RHUMATO (2019), vol. 17, n°4,
pp. 42–50
DOI: 10.xxxxxxxxxx
Status : Postprint (Author's version)

The resistance of the electrolyte is relatively low and in the same range for all electrodes ($R_e = \pm 3.5\Omega$) because the same electrolyte was used in the cell configuration. Regarding the charge transfer resistance, it can be observed that $R_{CT}$ is different for all electrodes which is due to the addition of the different carbon allotropes during the synthesis of the KVP/C materials. Indeed, the $R_{CT}$ of pristine KVP electrode is almost two times higher than of KVP/20CNT composite electrode.

Similar results are observed with the two other composite electrodes (KVP/20rGO and KVP/10CNT+10rGO) illustrating resistance values that are clearly lower than the $R_{CT}$ of KVP electrode. In summary, the EIS results suggest that the addition of carbon allotrope enhances the electronic conductivity which improved charge transfer reaction kinetics and leads to better cycling performance for KVP/C electrode materials with lower charge transfer resistance and optimized electrode-electrolyte interface in terms of ionic conduction.

## 3.6. INFLUENCE OF A BALL MILLING PROCESS ON THE STRUCTURAL AND MICROSTRUCTURAL PROPERTIES OF KVP AND KVP/C

With the aim to further enhance the electrochemical performance of the KVP and KVP/C materials, the powders were ground to decrease their particle size to about 100 nm and thus increase the surface area. The XRD patterns of the ground materials are indexed as pure KVP phase and reveal no crystallized impurity peaks (see Fig. 6a). However, peaks become broader and the peak area decreases after the milling process due to the amorphization. The decrease in average crystallite size after ball-milling process for KVP, KVP/20CNT and KVP/10CNT+10rGO is shown in Table 2 that is expected to be favorable for the electrochemical applications because in general, smaller crystallite size enhance the discharge/charge process during electrochemical cycling [13]. The crystallite size of KVP/20rGO is an exception and remains unchanged which suggests that the graphene layer formed on the surface of the KVP particles inhibited the decrease of the crystallite size by being itself broken during grinding (see later).

It is known that smaller and homogeneous active material particles are suitable for battery applications. In this section, the effect of the milling time on the particle size in KVP and KVP/C powders is investigated. The evolution of particle size with time was probed by laser granulometry. Fig. 6b, c, 6d and 6e present the particle-size distribution and SEM images of KVP and KVP/C after ball milling during 90 and 120 min (Fig. 6g–j). The powders have initially particles larger than 2.9 μm for KVP, KVP/20rGO and KVP/10CNT+10rGO and 6.5 μm for KVP/20CNT. A clear shift of the particle-size distribution toward lower values is observed after ball milling. The primary particle size for the ball-milled samples is reduced to about 100 nm after 90 min for KVP, KVP/20rGO and KVP/10CNT+10rGO. However, after 120 min the particles agglomerate and the apparent size increases to 2.9 μm for KVP/ 20rGO and KVP/10CNT+10rGO while the size distribution does not change much for KVP. After ball-milling during 90 min the compact rigid particles were crushed and transformed into small particles with pronounced reduction of the particle size; the boundaries between different particles are more distinguishable which leads to maximizing the surface area and formation of nano-sized powder particles. It is clear that KVP/20CNT required longer time of ball-milling (120 min) to decrease the particle size to 100 nm, which is due to the higher mechanical strength imparted by the homogeneous distribution of the carbon nanotubes inside and at the surface of KVP particles, which makes the milling process harder.

Published in : ORTHO-RHUMATO (2019), vol. 17, n°4,
pp. 42–50
DOI: 10.xxxxxxxxxx
Status : Postprint (Author's version)

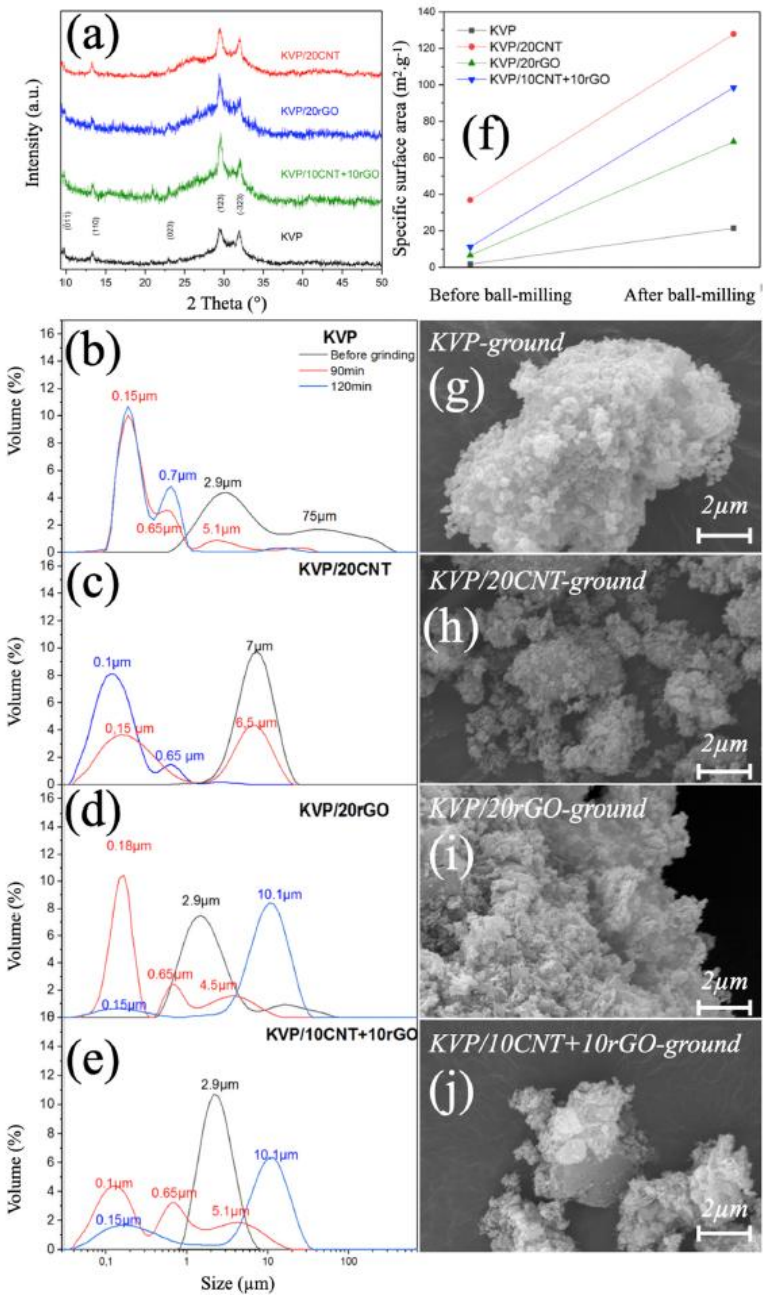


Fig. 6. (a) XRD patterns of KVP, KVP/ 20CNT, KVP/20rGO and KVP/ 10CNT+10rGO prepared by spray-drying with carbon allotropes, pyrolyzed at 650 °C for 8 h under argon, after grinding in isopropanol. Particle-size distribution during ball-milling process of (b) KVP, (c) KVP/ 20CNT, (d) KVP/20rGO and (e) KVP/ 10CNT+10rGO. (f) Evolution of the specific surface area of the KVP and KVP/C sample before and after ball-milling. SEM micrographs of (g) KVP, (h) KVP/20CNT, (i) KVP/ 20rGO and (j) KVP/10CNT+10rGO prepared by spray-drying with addition of carbon, after grinding in isopropanol.

Fig. 6c shows that after 90min of grinding the KVP/20CNT sample has a particle-size distribution with two major peaks at 0.15 µm and 6.5 µm of equivalent volume proportion. After 120min the KVP/20CNT sample is mainly composed of 100 nm particles. Relatively symmetric and narrow distribution curves were obtained for KVP, KVP/20rGO and KVP/20CNT after ball-milling which confirms a more homogeneous particle size distribution after grinding. A poly-dispersed distribution is obtained for KVP/10CNT+10rGO indicating inhomogeneous particle size distribution since the sample contains both large and small particles which could be due to the presence of two carbon types which leads to flattened 2D CNT/GO giving higher size. This result was confirmed by SEM micrographs (Fig. 6g–j). The composite materials with rGO (KVP/ 20rGO

Published in : ORTHO-RHUMATO (2019), vol. 17, n°4,
pp. 42–50
DOI: 10.xxxxxxxxxx
Status : Postprint (Author's version)

and KVP/10CNT+10rGO) are constituted by two sorts of particles; Small particles with rough and irregular surface and shape and the second sort with higher particle size made of blocks with regular flat surface.

The grinding process has a strong influence on the specific surface of the samples as shown in Fig. 6f. All milled samples demonstrated a significant increase in the specific surface area. The KVP/20CNT sample shows the highest specific surface area of 127.9 $m^2 g^{-1}$, thanks to the presence of CNT and the marked decrease in the particle size. The carbon-free KVP sample shows the lowest specific surface area (21.4 $m^2 g^{-1}$) amongst the ground samples, which is still 10 times higher than before grinding. The KVP/20rGO sample revealed also a tenfold increase of the specific surface after grinding (68.8 $m^2 g^{-1}$) and the mixed composite shows a specific surface area value between KVP/20CNT and KVP/20rGO with 98.5 $m^2 g^{-1}$.

## 3.7. INFLUENCE OF THE BALL MILLING PROCESS ON THE ELECTROCHEMICAL PROPERTIES OF KVP AND KVP/C

The KVP material is expected to deliver higher specific capacities after grinding thanks to smaller and homogeneous particle size of KVP. Galvanostatic tests were performed with a cycling rate of C/40 for the positive electrodes prepared from ground KVP and KVP/C within the voltage range 2–4.5 V as shown in Fig. 7a. The ground KVP, KVP/20rGO, KVP/20CNT and KVP/10CNT+10rGO delivered reversible capacities of around 60, 50, 101 and 60 $mAh.g^{-1}$, respectively. KVP and KVP/20CNT exhibited higher discharge capacities after grinding thanks to the decrease of their particle size and the increase of the specific surface area. However, the electrochemical performance of KVP/20rGO and KVP/10CNT+10rGO were lower than before grinding. Fig. 7b presents rate performance and Fig. 7c–f presents the galvanostatic charge–discharge voltage curves of the ground KVP and KVP/C positive electrodes obtained at various current densities from C/20 to 1C. The initial discharge capacities delivered by KVP, KVP/20rGO, KVP/20CNT and KVP/10CNT+10rGO are 53, 21, 73 and 64 $mAh.g^{-1}$, respectively. Similar to the result obtained at C/40, the sample with reduced graphene oxide after ball-milling shows the lowest capacity. In the case of KVP/20rGO the graphene layer breaks during the milling process resulting in heterogeneous carbon mixing with the KVP material; sluggish $K^+$ ion diffusion and high charge-transfer resistance leading to low discharge capacities at different current densities. This effect has been evidenced by EIS analysis. The Nyquist plots of KVP/20rGO before and after grinding from 1 MHz to 10 mHz are displayed in Fig. 8a. We can clearly see that the grinding step has deteriorated the rGO layer thus leading to a huge increase in the transfer charge resistance. The $R_{CT}$ almost doubled from 99Ω before grinding to 189Ω after grinding, which is almost the same value compared to the pristine KVP electrode (Table 3). This result confirms that rGO layer on KVP particles was destroyed during the grinding step, which leads to inferior electrochemical performance of the KVP/GO composite material.

As the current density increases, the discharge capacity in all four electrodes decreases due to polarization and kinetic limitations (Fig. 7b). The original delivered capacity of all samples is however restored when the cycling rate is reduced back to C/20, confirming the high structural stability of the KVP during the cycling even at high C-rate (1C). This result indicates that the capacity decay with increasing current density is induced by kinetic limitation. Indeed, the discharge capacity of electrode decreases much faster than that of the other electrodes due to its low electronic conductivity resulting in the rapid decrease of the discharge

Published in : ORTHO-RHUMATO (2019), vol. 17, n°4,
pp. 42–50
DOI: 10.xxxxxxxxxx
Status : Postprint (Author's version)

and charge voltage plateaus with increase of the current density. The ground KVP/20CNT material exhibits the best discharge capacities and rate capability compared to ground KVP, KVP/ 10CNT+10rGO and KVP/20rGO.

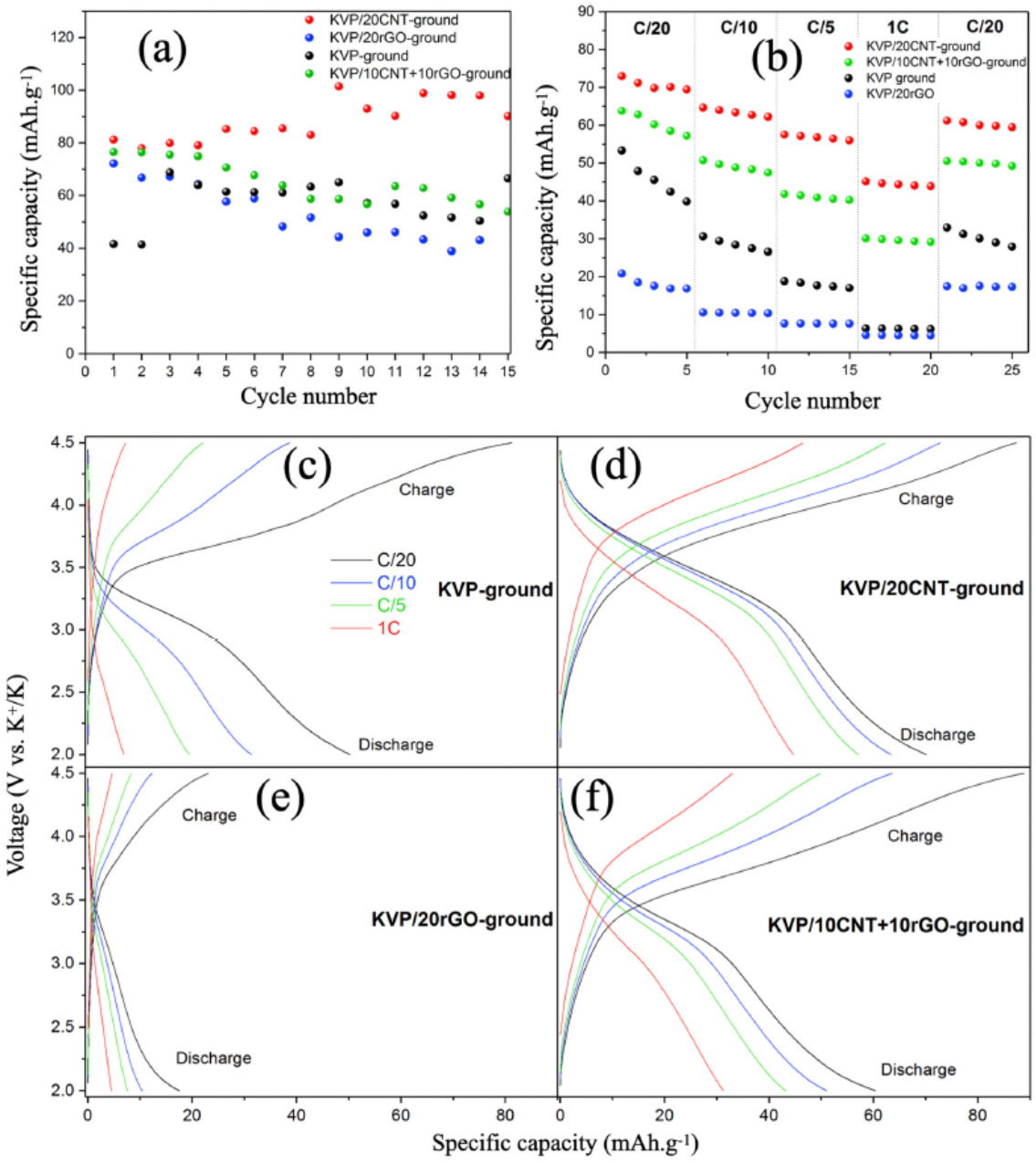


*Fig. 7. (a) Evolution of charge and discharge capacity vs. cycle number of the ground KVP, KVP/20CNT, KVP/20rGO and KVP/10CNT+10rGO materials at room temperature at C/40. The voltage window explored was 2.0–4.5 V. (b) Evolution of charge and discharge capacity vs. cycle number of the ground KVP, KVP/20CNT, KVP/20rGO and KVP/10CNT+10rGO materials cycled at C/20, C/10, C/5, 1C rates at room temperature. Charge/discharge curves of the first 3 cycles of (c) KVP, (d) KVP/20CNT, (e) KVP/20rGO and (f) KVP/10CNT+10rGO.*

Published in : ORTHO-RHUMATO (2019), vol. 17, n°4,
pp. 42–50
DOI: 10.xxxxxxxxxx
Status : Postprint (Author's version)

The ground KVP/20CNT electrode exhibits the best electrochemical performance which is due to the homogeneous particle-size distribution with small particles of about 100 nm. This induced an increase of the specific surface area (127.9 $m^2 g^{-1}$) as confirmed by BET measurements. Consequently, first the contact between the particle's surface and the electrolyte is increased which creates more active surface material and leads to fast ion diffusion pathways. Secondly the conductive carbon nanotube network facilitates rapid electron transport during charge/ discharge process which leads to improved electrochemical performance during cycling. Fig. 8b presents the cycling performance of ground KVP/ 20CNT electrode at a cycling rate of C/10 over 70 cycles. The initial specific discharge capacity was 80 $mAh.g^{-1}$ with a capacity retention of 82% and a corresponding coulombic efficiency of 96%. The galvanostatic results clearly showed that the ground KVP/20CNT positive electrode material exhibited good cyclability.

Cyclic voltammetry (CV) can be used to study the kinetics of the electrochemical reactions in the electrode material and the diffusion of $K^+$ ions. The CV tests were performed at different scan rates (0.1–0.5 m V $s^{-1}$) for KVP, KVP-ground, KVP/20CNT (Fig. S6) and KVP/20CNT- ground (Fig. 8c). For pure KVP, no redox peaks are observed which is in agreement with the poor electrochemical performance obtained for this cathode material. For the KVP-ground and KVP/CNT, low intensity oxidation and reduction peaks are observed. When the addition of carbon and the grinding of the material are combined, intense redox peaks are observed. This result confirms the superior performance achieved for the KVP/20CNT-ground sample. To study and compare the reaction kinetics of these materials, we plotted the current of the redox peaks versus the square root of the scan rate ($v^{1/2}$), it can be seen that these parameters have a linear relationship (Fig. 8d and Fig. S7). This indicates that the diffusion process is controlled by insertion/disinsertion of potassium for each electrode material. This relationship can be described by Randles-Sevcik equation [49][50][51].

$$I_p = (2.69E{+}5)\, n^{3/2}\, A\, (D_{K+})^{½}\, C_{K+}\, v^{½}$$

where $I_p$ is the peak current, n is the number of electrons, A is the effective surface area, $D_{K+}$ is the diffusion coefficient of potassium ion and $C_{K+}$ is the maximum concentration of $K^+$ ion in the electrode during electrochemical analysis.

The slope of the curves is reported in Table S2. As it can be observed the slope of oxidation current for both KVP-ground and KVP/20CNT electrodes are similar, contrary to the slope of the oxidation current in KVP/20CNT-ground electrode which is twice higher. As the number of electrons and the concentration are equivalent for these electrode materials, and that the diffusion of $K^+$ takes place through the same crystallographic structure for each sample (similar for each electrode), the difference between the current values is mainly related to the effective surface area between electrode and electrolyte. For KVP-ground and KVP-20CNT, as almost the same slope is obtained for the evolution of $I_p$ current, we can assume that the effect of the grinding of KVP and the presence of CNT in the spherical particles lead to almost the same active surface area between electrode and electrolyte. In the case of KVP/ 20CNT-ground, the grinding step and the addition of CNT have a cumulative effect on the increase of active surface area since the slope is twice higher for cathodic current and even ten times higher for the anodic current. This increase of active surface area is the main reason behind the superior electrochemical performance confirmed by the galvanostatic cycling results.

Published in : ORTHO-RHUMATO (2019), vol. 17, n°4,
pp. 42–50
DOI: 10.xxxxxxxxxx
Status : Postprint (Author's version)

# 4. Conclusions

$K_3V(PO_4)_2$ (KVP) and $K_3V(PO_4)_2$/C (KVP/C) pure materials have been successfully prepared by spray-drying followed by a heat treatment at 650 °C during 8 h under argon atmosphere. The as-obtained KVP compound exhibits low electrochemical performance due to low electronic conductivity associated to the anionic structure and also due to the large particle size and low specific surface of the spherical KVP particles, which limit the $K^+$ ions insertion reaction kinetics during cycling.

The in-situ addition of conductive carbon during spray-drying synthesis of KVP/C composite particles results in a large improvement of the specific capacity and enhanced capacity retention upon cycling. Indeed, the specific capacity obtained for KVP/20CNT and KVP/20rGO are doubled and tripled at C/40 compared to the original KVP electrode material. Grinding of the KVP and KVP/C particles induces an amorphization of the phase with significant reduction of the particle size and a homogeneous particle size distribution except for KVP/20rGO. The grinding step was actually found to be harmful for the two composites with rGO because the graphene layers that surround the KVP particles are broken. On the contrary, the KVP/20CNT composite electrode shows excellent electrochemical performance after ball-milling leading to high discharge capacity (101 $mAh.g^{-1}$ at C/40) and excellent capacity retention even at higher C-rates (C/20 to 1C).

# 5. Associated content

## SUPPORTING INFORMATION

The supporting information file contains: Table S1 Specific surface area of KVP and KVP/C sample, Fig. S1 Rietveld refinement of the KVP structure, Fig. S2 SEM micrographs of KVP before and after pyrolysis, Fig. S3 Charge discharge profile of KVP and cycling stability, Fig. S4 TEM micrograph of KVP/20rGO, Fig. S5 equivalent circuit model used to analyze the impedances spectra, Fig. S6 Cyclic voltammograms of KVP, KVP-ground and KVP/20CNT, Fig. S7 Evolution of peaks intensity versus the square root of the scan rate, Table S2 Slope of the linear fit curve from graphs of the evolution of peaks intensity versus the square root of the scan rate.

## CREDIT AUTHORSHIP CONTRIBUTION STATEMENT

**Jérôme Bodart:** Conceptualization, Validation, Formal analysis, Investigation, Writing - original draft, Visualization. **Nicolas Eshraghi:** Validation, Formal analysis, Writing - review & editing. **Thomas Carabin:** Validation, Investigation. **Bénédicte Vertruyen:** Formal analysis, Writing - review & editing. **Rudi Cloots:** Resources, Supervision, Funding acquisition. **Frederic Boschini:** Conceptualization, Resources, Supervision, Funding acquisition. **Abdelfattah Mahmoud:** Conceptualization, Formal analysis, Writing - original draft, Writing - review & editing.

Published in : ORTHO-RHUMATO (2019), vol. 17, n°4,
pp. 42–50
DOI: 10.xxxxxxxxxx
Status : Postprint (Author's version)

## DECLARATION OF COMPETING INTEREST

The authors declare that they have no known competing financial interests or personal relationships that could have appeared to influence the work reported in this paper.

## ACKNOWLEDGMENT

The authors are grateful to University of Liege and FRS-FNRS for equipment grants. The authors are grateful to the Walloon region for the support under "PE PlanMarshall2.vert" program (BATWAL – 1318146) and a Beware Fellowship Academia 2015–1, RESIBAT n° 1510399. N.E. thanks FNRS for the PhD FRIA grant [Grant 1.E118.16].

## APPENDIX A. SUPPLEMENTARY DATA

Supplementary data to this article can be found online at https://doi. org/10.1016/j.jpowsour.2020.229057.

## AUTHOR CONTRIBUTIONS

The manuscript was written through contributions of all authors. All authors have given approval to the final version of the manuscript.

## REFERENCES

[1] N. Yabuuchi, K. Kubota, M. Dahbi, S. Komaba, Research development on sodium- ion batteries, Chem. Rev. 114 (2014) 11636–11682, https://doi.org/10.1021/ cr500192f.

[2] K. Kubota, M. Dahbi, T. Hosaka, S. Kumakura, S. Komaba, Towards K-ion and Na- ion batteries as "beyond Li-ion, Chem. Rec. 18 (2018) 459–479, https://doi.org/ 10.1002/tcr.201700057.

[3] X. Wu, D.P. Leonard, X. Ji, Emerging non-aqueous potassium-ion batteries: challenges and opportunities, Chem. Mater. 29 (2017) 5031–5042, https://doi. org/10.1021/acs.chemmater.7b01764.

[4] H. Kim, J.C. Kim, M. Bianchini, D.H. Seo, J. Rodriguez-Garcia, G. Ceder, Recent progress and perspective in electrode materials for K-ion batteries, Adv. Energy Mater. 8 (2018) 1–19, https://doi.org/10.1002/aenm.201702384.

[5] S. Komaba, T. Hasegawa, M. Dahbi, K. Kubota, Potassium intercalation into graphite to realize high-voltage/high-power potassium-ion batteries and potassium-ion capacitors, Electrochem. Commun. 60 (2015) 172–175, https://doi.org/10.1016/j.elecom.2015.09.002.

[6] X. Bie, K. Kubota, T. Hosaka, K. Chihara, S. Komaba, A novel K-ion battery: hexacyanoferrate(ii)/graphite cell, J. Mater. Chem. A. 5 (2017) 4325–4330, https://doi.org/10.1039/c7ta00220c.

[7] Y. Chen, W. Luo, M. Carter, L. Zhou, J. Dai, K. Fu, S. Lacey, T. Li, J. Wan, X. Han, Y. Bao, L. Hu, Organic electrode for non-aqueous potassium-ion batteries, Nanomater. Energy 18 (2015) 205–211, https://doi.org/10.1016/j. nanoen.2015.10.015.

[8] Y. Hironaka, K. Kubota, S. Komaba, P2- and P3-KxCoO2 as an electrochemical potassium intercalation host, Chem. Commun. 53 (2017) 3693–3696, https://doi. org/10.1039/c7cc00806f.

[9] B. Huang, Y. Shao, Y. Liu, Z. Lu, X. Lu, S. Liao, Improving potassium-ion batteries by optimizing the composition of prussian blue cathode, ACS Appl. Energy Mater. 2 (2019) 6528–6535, https://doi.org/10.1021/acsaem.9b01097.

Published in : ORTHO-RHUMATO (2019), vol. 17, n°4,
pp. 42–50
DOI: 10.xxxxxxxxxx
Status : Postprint (Author's version)

[10] G. He, L.F. Nazar, Crystallite size control of prussian white analogues for nonaqueous potassium-ion batteries, ACS Energy Lett 2 (2017) 1122–1127, https://doi.org/10.1021/acsenergylett.7b00179.

[11] X. Wang, X. Xu, C. Niu, J. Meng, M. Huang, X. Liu, Z. Liu, L. Mai, Earth abundant Fe/Mn-based layered oxide interconnected nanowires for advanced K-ion full batteries, Nano Lett. 17 (2017) 544–550, https://doi.org/10.1021/acs. nanolett.6b04611.

[12] T. Jungers, A. Mahmoud, C. Malherbe, F. Boschini, B. Vertruyen, Sodium iron sulfate alluaudite solid solution for Na-ion batteries: moving towards stoichiometric Na2Fe2(SO4)3, J. Mater. Chem. A. 7 (2019) 8226–8233, https:// doi.org/10.1039/c9ta00116f.

[13] N. Eshraghi, S. Caes, A. Mahmoud, R. Cloots, B. Vertruyen, F. Boschini, Sodium vanadium (III) fluorophosphate/carbon nanotubes composite (NVPF/CNT) prepared by spray-drying: good electrochemical performance thanks to well- dispersed CNT network within NVPF particles, Electrochim. Acta 228 (2017) 319–324, https://doi.org/10.1016/j.electacta.2017.01.026.

[14] M. Brisbois, S. Caes, M.T. Sougrati, B. Vertruyen, A. Schrijnemakers, R. Cloots, N. Eshraghi, R.P. Hermann, A. Mahmoud, F. Boschini, Na2FePO4F/multi-walled carbon nanotubes for lithium-ion batteries: operando Mossbauer study of spray- ¨ dried composites, Sol. Energy Mater. Sol. Cells 148 (2016) 67–72, https://doi.org/ 10.1016/j.solmat.2015.09.005.

[15] A. Mahmoud, S. Caes, M. Brisbois, R.P. Hermann, L. Berardo, A. Schrijnemakers, C. Malherbe, G. Eppe, R. Cloots, B. Vertruyen, F. Boschini, Spray-drying as a tool to disperse conductive carbon inside Na2FePO4F particles by addition of carbon black or carbon nanotubes to the precursor solution, J. Solid State Electrochem. (2017), https://doi.org/10.1007/s10008-017-3717-x.

[16] V. Mathew, S. Kim, J. Kang, J. Gim, J. Song, J.P. Baboo, W. Park, D. Ahn, J. Han, L. Gu, Y. Wang, Y.S. Hu, Y.K. Sun, J. Kim, Amorphous iron phosphate: potential host for various charge carrier ions, NPG Asia Mater. 6 (2014), https://doi.org/ 10.1038/am.2014.98.

[17] B. Senthilkumar, R.K. Selvan, P. Barpanda, Potassium-ion intercalation in anti- NASICON-type iron molybdate Fe2(MoO4)3, Electrochem, Commun. Now. 110 (2020) 106617, https://doi.org/10.1016/j.elecom.2019.106617.

[18] J. Liao, Q. Hu, J. Mu, X. He, S. Wang, C. Chen, A vanadium-based metal-organic phosphate framework material K 2 [(VO) 2 (HPO 4 ) 2 (C 2 O 4 )] as a cathode for potassium-ion batteries, Chem. Commun. 55 (2019) 659–662, https://doi.org/ 10.1039/c8cc08734b.

[19] S. Zheng, S. Cheng, S. Xiao, L. Hu, Z. Chen, B. Huang, Q. Liu, J. Yang, Q. Chen, Partial replacement of K by Rb to improve electrochemical performance of K3V2 (PO4)3 cathode material for potassium-ion batteries, J. Alloys Compd. 815 (2020) 152379, https://doi.org/10.1016/j.jallcom.2019.152379.

[20] X. Lin, J. Huang, H. Tan, J. Huang, B. Zhang, K3V2(PO4)2F3as a robust cathode for potassium-ion batteries, Energy Storage Mater 16 (2019) 97–101, https://doi.org/ 10.1016/j.ensm.2018.04.026.

[21] L. Zhang, B. Zhang, C. Wang, Y. Dou, Q. Zhang, Y. Liu, H. Gao, M. Al-Mamun, W. K. Pang, Z. Guo, S.X. Dou, H.K. Liu, Constructing the best symmetric full K-ion battery with the NASICON-type K 3 V 2 (PO 4 ) 3, Nanomater. Energy 60 (2019) 432–439, https://doi.org/10.1016/j.nanoen.2019.03.085.

[22] J. Han, Y. Niu, S.J. Bao, Y.N. Yu, S.Y. Lu, M. Xu, Nanocubic KTi2(PO4)3 electrodes for potassium-ion batteries, Chem. Commun. 52 (2016) 11661–11664, https://doi. org/10.1039/c6cc06177j.

[23] T. Hosaka, T. Shimamura, K. Kubota, S. Komaba, Polyanionic compounds for potassium-ion batteries, Chem. Rec. 19 (2019) 735–745, https://doi.org/10.1002/ tcr.201800143.

[24] L. Lander, G. Rousse, A.M. Abakumov, M. Sougrati, G. Van Tendeloo, J. M. Tarascon, Structural, electrochemical and magnetic properties of a novel KFeSO4F polymorph, J. Mater. Chem. A. 3 (2015) 19754–19764, https://doi.org/ 10.1039/c5ta05548b.

[25] N. Recham, G. Rousse, M.T. Sougrati, J.N. Chotard, C. Frayret, S. Mariyappan, B.

Published in : ORTHO-RHUMATO (2019), vol. 17, n°4,
pp. 42–50
DOI: 10.xxxxxxxxxx
Status : Postprint (Author's version)

C. Melot, J.C. Jumas, J.M. Tarascon, Preparation and characterization of a stable FeSO4F-based framework for alkali ion insertion electrodes, Chem. Mater. 24 (2012) 4363–4370, https://doi.org/10.1021/cm302428w.

[26] W.B. Park, S.C. Han, C. Park, S.U. Hong, U. Han, S.P. Singh, Y.H. Jung, D. Ahn, K. S. Sohn, M. Pyo, KVP2O7 as a robust high-energy cathode for potassium-ion batteries: pinpointed by a full screening of the inorganic registry under specific search conditions, Adv. Energy Mater. 8 (2018) 1–12, https://doi.org/10.1002/ aenm.201703099.

[27] N.S. Katorova, S.S. Fedotov, D.P. Rupasov, N.D. Luchinin, B. Delattre, Y.M. Chiang, A.M. Abakumov, K.J. Stevenson, Effect of concentrated diglyme-based electrolytes on the electrochemical performance of potassium-ion batteries, ACS Appl. Energy Mater. 2 (2019) 6051–6059, https://doi.org/10.1021/acsaem.9b01173.

[28] K. Chihara, A. Katogi, K. Kubota, S. Komaba, KVPO4F and KVOPO4 toward 4 volt- class potassium-ion batteries, Chem. Commun. 53 (2017) 5208–5211, https://doi. org/10.1039/c6cc10280h

[29] S.S. Fedotov, N.R. Khasanova, A.S. Samarin, O.A. Drozhzhin, D. Batuk, O. M. Karakulina, J. Hadermann, A.M. Abakumov, E.V. Antipov, AVPO4F (A = Li, K): a 4 v cathode material for high-power rechargeable batteries, Chem. Mater. 28 (2016) 411–415, https://doi.org/10.1021/acs.chemmater.5b04065.

[30] N. Goubard-Bretesch´e, E. Kemnitz, N. Pinna, A general low-temperature synthesis route to polyanionic vanadium phosphate fluoride cathode materials: AVPO 4 F (A = Li, Na, K) and Na 3 V 2 (PO 4 ) 2 F 3, Mater. Chem. Front. 3 (2019) 2164–2174, https://doi.org/10.1039/c9qm00325h.

[31] H. Kim, D.H. Seo, M. Bianchini, R.J. Cl´ement, H. Kim, J.C. Kim, Y. Tian, T. Shi, W. S. Yoon, G. Ceder, A new strategy for high-voltage cathodes for K-ion batteries: stoichiometric KVPO4F, Adv. Energy Mater. 8 (2018) 1–12, https://doi.org/ 10.1002/aenm.201801591.

[32] V.A. Nikitina, S.M. Kuzovchikov, S.S. Fedotov, N.R. Khasanova, A.M. Abakumov, E. V. Antipov, Effect of the electrode/electrolyte interface structure on the potassium- ion diffusional and charge transfer rates: towards a high voltage potassium-ion battery, Electrochim. Acta 258 (2017) 814–824, https://doi.org/10.1016/j. electacta.2017.11.131.

[33] L. Benhamada, A. Grandin, M.M. Borel, A. Leclaire, B. Raveau, A new vanadium III potassium phosphate with a cage structure: K6V2P4O16, J. Solid State Chem. 91 (1991) 264–270, https://doi.org/10.1016/0022-4596(91)90080-2.

[34] X. Wang, C. Niu, J. Meng, P. Hu, X. Xu, X. Wei, L. Zhou, K. Zhao, W. Luo, M. Yan, L. Mai, Novel K3V2(PO4)3/C bundled nanowires as superior sodium-ion battery electrode with ultrahigh cycling stability, Adv. Energy Mater. 5 (2015) 1–8, https://doi.org/10.1002/aenm.201500716.

[35] R.W. Cheary, A. Coelho, Fundamental parameters approach to x-ray line-profile fitting, J. Appl. Crystallogr. 25 (1992) 109–121, https://doi.org/10.1107/ S0021889891010804.

[36] A. Bernard, Boukamp, A package for impedance/admittance data analysis, Solid State Ionics 18&19 (1986) 136–140, https://doi.org/10.1017/ CBO9781107415324.004.

[37] A. Mahmoud, I. Saadoune, S. Difi, M.T. Sougrati, P.E. Lippens, J.M. Amarilla, Study of the structural and thermal stability of Li0.3Co 2/3Ni1/6Mn1/6O2, Electrochim. Acta 135 (2014) 536–542, https://doi.org/10.1016/j.electacta.2014.05.058.

[38] R.S. Viswanath, P.J. Miller, High temperature phase transition in NH4H2PO4, Solid State Commun. 32 (1979) 703–706, https://doi.org/10.1016/0038-1098(79) 90733-6.

[39] A. Marcilla, A. Gomez-Siurana, M. Beltr´ an, I. Martínez-Castellanos, I. Blasco, ´ D. Berenguer, TGA-FTIR study of the pyrolysis of sodium citrate and its effect on the pyrolysis of tobacco and tobacco/SBA-15 mixtures under N2 and air atmospheres, J. Sci. Food Agric. 98 (2018) 5916–5931, https://doi.org/10.1002/ jsfa.9121.

[40] T. Kavinkumar, S. Manivannan, Synthesis, characterization and gas sensing properties of graphene oxide-multiwalled carbon nanotube composite, J. Mater. Sci. Technol. 32 (2016) 626–632, https://doi.org/10.1016/j.jmst.2016.03.017.

Published in : ORTHO-RHUMATO (2019), vol. 17, n°4,
pp. 42–50
DOI: 10.xxxxxxxxxx
Status : Postprint (Author's version)

[41] H.H. Huang, K.K.H. De Silva, G.R.A. Kumara, M. Yoshimura, Structural evolution of hydrothermally derived reduced graphene oxide, Sci. Rep. 8 (2018) 2–10, https://doi.org/10.1038/s41598-018-25194-1.

[42] X. Qiao, S. Liao, C. You, R. Chen, Phosphorus and nitrogen dual doped and simultaneously reduced graphene oxide with high surface area as efficient metal- free electrocatalyst for oxygen reduction, Catalysts 5 (2015) 981–991, https://doi. org/10.3390/catal5020981.

[43] F. Cheng, Z. Tao, J. Liang, J. Chen, Template-directed materials for rechargeable lithium-ion batteries, Chem. Mater. 20 (2008) 667–681, https://doi.org/10.1021/ cm702091q.

[44] C. Karegeya, A. Mahmoud, R. Cloots, B. Vertruyen, F. Boschini, Hydrothermal synthesis in presence of carbon black: particle-size reduction of iron hydroxyl phosphate hydrate for Li-ion battery, Electrochim. Acta 250 (2017) 49–58, https:// doi.org/10.1016/j.electacta.2017.08.006.

[45] A. Mahmoud, S. Caes, M. Brisbois, R.P. Hermann, L. Berardo, A. Schrijnemakers, C. Malherbe, G. Eppe, R. Cloots, B. Vertruyen, F. Boschini, Spray-drying as a tool to disperse conductive carbon inside Na2FePO4F particles by addition of carbon black or carbon nanotubes to the precursor solution, J. Solid State Electrochem. 22 (2018) 103–112, https://doi.org/10.1007/s10008-017-3717-x.

[46] P. Seydel, J. Blomer, J. Bertling, Modeling particle formation at spray drying using ¨ population balances, Dry. Technol. 24 (2006) 137–146, https://doi.org/10.1080/ 07373930600558912.

[47] C. Karegeya, A. Mahmoud, R. Cloots, B. Vertruyen, F. Boschini, Hydrothermal synthesis in presence of carbon black: particle-size reduction of iron hydroxyl phosphate hydrate for Li-ion battery, Electrochim. Acta 250 (2017) 49–58, https:// doi.org/10.1016/j.electacta.2017.08.006.

[48] A. Mahmoud, M. Chamas, P.E. Lippens, Electrochemical impedance study of the solid electrolyte interphase in MnSn2 based anode for Li-ion batteries, Electrochim. Acta 184 (2015) 387–391, https://doi.org/10.1016/j.electacta.2015.10.078.

[49] C. Zhu, C. Wu, C. Chen, P. Kopold, P.A. Van Aken, J. Maier, A high power − high energy Na 3 V 2 ( PO 4 ) 2 F 3 sodium Cathode : investigation of transport parameters, Rational Design and Realization 2 (2017) 1–14, https://doi.org/ 10.1021/acs.chemmater.7b00927.

[50] K. Wang, R. Cai, T. Yuan, X. Yu, R. Ran, Z. Shao, Process investigation, electrochemical characterization and optimization of LiFePO4/C composite from mechanical activation using sucrose as carbon source, Electrochim. Acta 54 (2009) 2861–2868, https://doi.org/10.1016/j.electacta.2008.11.012.

[51] W.L. Liu, J.P. Tu, Y.Q. Qiao, J.P. Zhou, S.J. Shi, X.L. Wang, C.D. Gu, Optimized performances of core-shell structured LiFePO4/C nanocomposite, J. Power Sources 196 (2011) 7728–7735, https://doi.org/10.1016/j.jpowsour.2011.05.046.